

The evolution of continental roots in numerical thermo-chemical mantle convection models including differentiation by partial melting

J.H. de Smet ^{*}, A.P. van den Berg ¹, N.J. Vlaar ²

Department of Theoretical Geophysics, University of Utrecht, PO Box 80.021, 3508 TA Utrecht, The Netherlands

Received 30 April 1998; received in revised form 21 January 1999; accepted 25 January 1999

Abstract

Incorporating upper mantle differentiation through decompression melting in a numerical mantle convection model, we demonstrate that a compositionally distinct root consisting of depleted peridotite can grow and remain stable during a long period of secular cooling. Our modeling results show that in a hot convecting mantle partial melting will produce a compositional layering in a relatively short time of about 50 Ma. Due to secular cooling mantle differentiation finally stops before 1 Ga. The resulting continental root remains stable on a billion year time scale due to the combined effects of its intrinsically lower density and temperature-dependent rheology. Two different parameterizations of the melting phase-diagram are used in the models. The results indicate that during the Archaean melting occurred on a significant scale in the deep regions of the upper mantle, at pressures in excess of 15 GPa. The compositional depths of continental roots extend to 400 km depending on the potential temperature and the type of phase-diagram parameterization used in the model. The results reveal a strong correlation between lateral variations of temperature and the thickness of the continental root. This shows that cold regions in cratons are stabilized by a thick depleted root. © 1999 Elsevier Science B.V. All rights reserved.

Keywords: Thermo-chemical convection; Numerical modeling; Upper mantle differentiation; Continental evolution; Partial melting; Continental root

1. Introduction

Continental nuclei are much older than oceanic lithosphere. Continents have cratonic segments with ages of 3.0 billion years and older (Condie, 1984), in contrast with the oceanic lithosphere with ages up to about 200 million years (Müller et al., 1996). Thus,

continents apparently form stable systems in the sense that they do not subduct. Oceanic lithosphere is subducting at ocean-continent boundaries, and this process is relatively well understood. The evolution of continental systems is much less clear. In this paper, we present a model for the formation and long term evolution of continental systems within the framework of a numerical mantle convection model.

There exists evidence for a specific continental configuration that extends to several hundreds of kilometers into the upper mantle. It has been suggested that the continental lithosphere, also called the

^{*} Corresponding author. E-mail: smet@geo.uu.nl; fax: +31-30-253-50-30

¹ E-mail: berg@geo.uu.nl.

² E-mail: vlaar@geo.uu.nl.

tectosphere (Jordan, 1975), is a cold layer that is prevented from collapsing through a compositionally determined low intrinsic density. An overview of evidence supporting such a chemically distinct layer is given by Jordan (1988). Estimates of the depths of these chemically defined continental roots range from 200–400 km (Jordan, 1975, 1988; Anderson, 1990; Polet and Anderson, 1995; Doin et al., 1996).

During the Archaean era the Earth had a hotter upper mantle because radiogenic heat production was higher and more initial heat from planetary formation and early differentiation was still stored in the Earth. It has been demonstrated that a hotter geotherm has a large effect on the depth where pressure release partial melting starts in the upper mantle (McKenzie, 1984). This melting process results in residual material with an intrinsically lower density and a basaltic crust derived from the primary melt. This low density residual material is depleted peridotite or harzburgite and its presence can explain the long term stability of ancient, i.e., > 3 Ga, continental areas through gravitationally stable compositional layering.

The importance of a higher mantle temperature to the stability of oceanic and continental lithospheric systems has been discussed in Vlaar and Van Den Berg (1991), Vlaar et al. (1994) who used simple models based on the 1-D adiabatic model for partial melting by McKenzie (1984). The results of these 1-D models showed that the present day style of plate tectonics cannot be extrapolated to the Archaean, since the compositionally differentiated layers produced by a convecting mantle must have been much thicker during the Archaean. It was shown that a thick layer of harzburgitic residue underneath an also thicker crust must have led to a different thermo-chemical convection regime (Vlaar et al., 1994). In this paper, we extend these earlier models of partial melting to non-adiabatic conditions within a thermo-chemical mantle convection model (Dupeyrat et al., 1995; De Smet et al., 1998a). We use a fully dynamical numerical mantle convection model including partial melting phase-diagrams based on empirical data. A similar model has been used by De Smet et al. (1998a) and it has been further extended to investigate continental evolution. A new more realistic parameterization of the melting phase-diagram is incorporated in the present work

allowing deep melting for a realistic young Earth continental geotherm. Here, we apply this dynamic mantle differentiation model to investigate an upper mantle system subject to secular cooling in a continental setting and study in particular the formation and subsequent thermo-chemical evolution of the continental root.

Other workers have investigated continental systems in the context of mantle convection models. Effects of rheology have been studied by Moresi and Solomatov (1997) and Schmeling and Bussod (1996). Effects of composition and rheology on delamination of a lithospheric root are studied by Schott and Schmeling (1998). Several authors use ad hoc compositional layering of the continental upper mantle. Lenardic (1997) uses this type of model to explain surface heat flow data. Stability aspects are examined by Doin et al. (1997). Long-term evolutions for the whole upper mantle including partial melting are examined by Ogawa (1994) and Kameyama et al. (1996). Walzer and Hendel (1997) included the lower mantle in their study of mantle evolution with respect to the chemical differentiation of heat-producing elements. The Hawaiiin hotspot and rifting scenarios in relation with partially melting mantle plumes are studied by Ribe and Christensen (1994), Ebinger and Sleep (1998), and Leitch et al. (1998).

In Section 2 we present our model which focuses on the Archaean continental upper mantle. Incorporated are several important physical aspects, such as adiabatic compression, viscous heating, time- and depth-dependent radiogenic heat generation, latent heat consumption, and a pressure- and temperature-dependent rheology.

2. The model

We have applied a numerical convection model for the upper mantle including pressure release melting. A similar model with a different parameterization of the melting phase diagram was applied by De Smet et al. (1998a).

2.1. Conceptual continental model

Fig. 1 gives a schematic depth profile of the model. The model incorporates a crust of 30 to 50

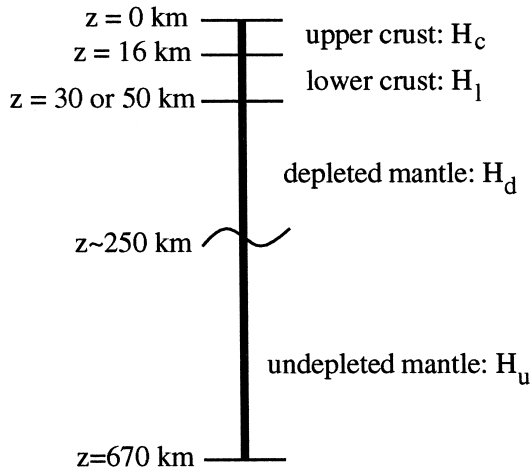


Fig. 1. Schematic depth profile of the continental model within the left-hand column depths in km. The upper and lower crust form a high density of viscosity layer with high radiogenic heat sources. The upper part of the mantle consists of a depleted layer up to approximately 250 km depending on the mantle temperature and in the present context also depending on the type of parameterization of the melting phase diagram (see Fig. 2). This depleted layer has an intrinsically lower density ($\rho(F > 0) < \rho_s$) than the deeper undepleted part of the upper mantle ($\rho(F = 0) = \rho_s$).

km thickness overlaying the upper mantle to a depth of 670 km, which is assumed to be mechanically decoupled from the lower mantle. The upper mantle consists of two layers: a deep lherzolitic layer of undepleted mantle peridotite and a more shallow harzburgitic layer with a variable degree of depletion. The depleted residual material is produced when the lherzolitic source material crosses its solidus and partial melting produces a melt fraction, which is assumed to be extracted instantaneously.

The process of partial melting also effects the distribution of radiogenic heat sources $H(\vec{x}, t)$. Fig. 1 gives a schematic depth profile of the model

distinguishing four layers with distinct values for $H(\vec{x}, t)$. The deeper undepleted mantle has an $H_u = 0.09 \mu\text{W m}^{-3}$, while the partial melting process reduces the value for the depleted layer to $H_d = 0.04$ or $0.0 \mu\text{W m}^{-3}$. This is due to the extraction of heat-producing incompatible elements (Walzer and Hendel, 1997). We used $H_l = 0.9 \mu\text{W m}^{-3}$ in the lower and $H_c = 4.13 \mu\text{W m}^{-3}$ in the upper crust. The values have been derived from the present day values given by O’Connell and Hager (1980) and Chapman (1986) by applying an amplification factor of two accounting for the mean radiogenic decay since the Archaean.

Estimations of Archaean radiogenic heat sources vary from two to three times the present day value. We have adopted the lower bound of this density range and included a decrease of productivity through the radioactive decay constant $\lambda = 0.347 \text{ Ga}^{-1}$, which corresponds to a half-life time of 2 Ga (Turcotte and Schubert, 1982).

Three different models A to C will be discussed. Model A and B have the heat generation parameterization mentioned above, whereas Model C has zero heat generation when the degree of depletion is larger than zero, i.e., $H_d = 0$ when $F > 0$. Both Models A and B have a crustal thickness of 50 km, whereas Model C has a reduced crustal thickness of 30 km. Further differences between the Models A to C are discussed below and an overview of the model characteristics is given in Table 1.

The high crustal heat generation values result in a significant crustal blanketing effect. Since the model crust also has a low density ($\rho_c = 3000 \text{ kg m}^{-3}$) and a high viscosity ($\eta_{\text{max}} = 10^{24} \text{ Pa s}$) it is stably situated on top of the continental mantle. Given the constant temperature at the surface (T_{srf}), the shallow geotherm in the Mechanical Boundary Layer (MBL)

Table 1

Differences between models A, B and C. The last column refers to the two initial geotherms given in Fig. 2a which are both warm and cold is meant in a relative way. The heat generation density for depleted material is given in column four (H_d). All model differences are discussed in Section 2

| Model | Crustal thickness (km) | Thermal coupling upper/lower mantle | H_d (mW m^{-3}) | Phase-diagram parameterization | Initial geotherm |
|-------|------------------------|-------------------------------------|------------------------------|--------------------------------|------------------|
| A | 50 | reservoir | 0.04 | linear | ‘hot’ |
| B | 50 | isolated | 0.04 | polynomial | ‘hot’ |
| C | 30 | isolated | 0.0 | polynomial | ‘cold’ |

at the top of the model is to a large extent determined by its heat source distributions.

In the deeper region, the geotherm is influenced by several other factors. One of them is the compositional layering. The formation of a depleted low density layer impedes large scale convection and the formation of an adiabatic mantle geotherm at this depth level. An additional factor is the rheological parameterization including a strong temperature dependence of the viscosity. The effect of cooling from the top is a strong increase of the viscosity which

gradually reduces the vigor of convection in the depleted zone which becomes stagnant from the top down.

We have used a Newtonian temperature- and pressure-dependent rheology. The viscosity model follows an Arrhenius relation which, in its dimensional form, is:

$$\eta(p, T) = \mathcal{B} \exp\left[\frac{E + pV}{RT}\right] \quad (1)$$

where values are given in Table 2 and the viscosity

Table 2
Explanation of used symbols

| Symbols | Definition | Value | Units |
|----------------------------------|---|-----------------------|-----------------------------------|
| α | Thermal expansion coefficient | 3×10^{-5} | K^{-1} |
| ρ_0 | Reference density | 3416 | kg m^{-3} |
| ρ | Effective density $\rho(T, F)$ | – | kg m^{-3} |
| ρ_c | Crustal density at $T = T_{\text{srf}}$ | 3000 | kg m^{-3} |
| $\delta \rho$ | Density drop upon full differentiation | 226 | kg m^{-3} |
| η | Non-dimensional viscosity | – | – |
| η_0 | Reference viscosity | 10^{21} | Pa s |
| η_{max} | Maximum viscosity | 10^{24} | Pa s |
| E | Activation energy | 250 | kJ mol^{-1} |
| V | Activation volume | 11.0 | $\mu\text{m}^3 \text{mol}^{-1}$ |
| R | Gas constant | 8.3143 | $\text{J mol}^{-1} \text{K}^{-1}$ |
| \mathcal{B} | Viscosity pre-factor | 9×10^{11} | Pa s |
| F | Degree of depletion | – | – |
| \vec{u} | Velocity | – | m s^{-1} |
| T | Non-dimensional temperature | – | – |
| q | Heat-flow | – | W m^{-2} |
| $\langle X \rangle_{\text{hor}}$ | Horizontally averaged quantity X | – | – |
| ΔT | Temperature scale | 2200 | K |
| T_{srf} | Surface temperature | 273.15 | K |
| T_0 | Non-dimensional surface temperature $T_{\text{srf}}/\Delta T$ | 0.12416 | – |
| $T_s(p)$ | Pressure-dependent solidus temperature | – | K |
| $T_l(p)$ | Pressure-dependent liquidus temperature | – | K |
| $\Delta T(p)_{\text{sl}}$ | Distance between solidus and liquidus | – | K |
| p | Pressure | – | Pa |
| Δp | Non-dimensional hydrodynamic pressure | – | – |
| h | Depth scale | 670 | km |
| λ | Radioactive decay constant | 0.347 | $(\text{Ga})^{-1}$ |
| κ | Thermal diffusivity | 10^{-6} | $\text{m}^2 \text{s}^{-1}$ |
| k | Thermal conductivity | 3.416 | $\text{W m}^{-1} \text{K}^{-1}$ |
| c_p | Heat capacity at constant pressure | 1000 | $\text{J kg}^{-1} \text{K}^{-1}$ |
| ΔS | Entropy change upon melting | 300 | $\text{J kg}^{-1} \text{K}^{-1}$ |
| H | Non-dimensional radiogenic heat generation | – | – |
| H_0 | Reference value radiogenic heat generation | 5.33×10^{-6} | W m^{-3} |
| Φ | Viscous dissipation | – | W m^{-3} |
| \mathcal{R} | Internal heating number: $H_0(h^2)/(k\Delta T)$ | 318.4 | – |
| Di | Dissipation number: $\alpha gh/c_p$ | 0.1970 | – |
| R_b | Compositional Rayleigh number $\delta \rho gh^3/\kappa\eta_0$ | 0.6661×10^6 | – |
| R_a | Thermal Rayleigh number: $\rho_0 \alpha \Delta T gh^3/\kappa\eta_0$ | 0.6645×10^6 | – |

is truncated at its maximum value $\eta_{\max} = 10^{24}$ Pa s which equates the crustal value. The viscosity pre-factor \mathcal{B} is determined from the constraint that at $z = 400$ km and $T = 2023.15$ K (i.e., 1750°C) the viscosity equals the reference viscosity value $\eta_0 = 10^{21}$ Pas. In the present models we apply a stronger pressure dependence of the rheology, expressed in a activation volume of $V = 11.0 \mu\text{m}^3 \text{mol}^{-1}$ compared to a $V = 7.5 \mu\text{m}^3 \text{mol}^{-1}$ used by De Smet et al. (1998a). Both numbers are in the range of possible values for the upper mantle (Ranalli, 1991; Karato and Wu, 1993). The increase of the pressure dependence increases the viscosity mainly in the deeper parts of the model, whereas at shallower depth the mobility increases and the zone of minimum viscosity occurs at shallower depth ($z = 80$ km at $t = 0$ in the present Models A and B). This results in a thinner MBL and an overall decrease of the geotherm of about 175 K. We consider the reduced maximum temperature in the present models to be more representative for the young Earth. The horizontally averaged geotherm for $t = 0$ for Models A and B used here is depicted as the thick dotted line in Fig. 2a. The thin dotted line in Fig. 2a is the colder horizontally averaged geotherm corresponding to Model C. The difference is caused by the thinner crust in Model C.

In mantle peridotites subject to partial melting, the solubility of water is higher in the basaltic melt fraction than in olivine. Furthermore, hydrous olivine has a lower viscosity than anhydrous olivine. Thus, basaltic melt extraction will increase the viscosity of the residual material (Karato, 1990; Karato and Jung, 1998; Hirth and Kohlstedt, 1996). This effect can amount up to two orders of magnitude as estimated by Karato and Jung (1998). The influence of a modest increase in viscosity, i.e., the viscosity change of almost dry olivine to dry olivine, on the model has been investigated by De Smet et al. (1998a). It stabilizes the root further and increases the thermal blanketing effect slightly.

The initial geotherm has been computed from the resulting temperature field obtained from a startup convection run. In this startup run, partial melting and the decrease of heat production in time are artificially switched off. After several hundred million years a statistically steady-state sets in, and a single snapshot of the temperature field of this

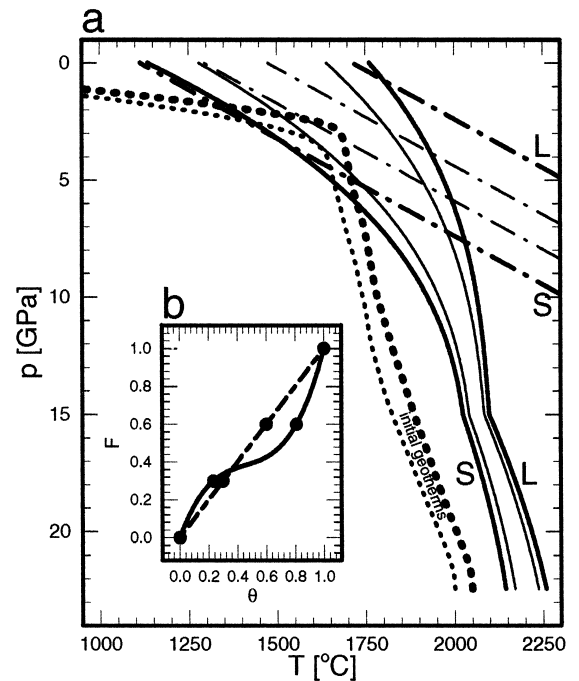


Fig. 2. Parameterizations used in the models. (a) The thick lines are the solidus and liquidus for the linear (dashed) and polynomial (solid) parameterization where *S* and *L* indicate the solidus and liquidus for both parameterizations, respectively. The thinner lines correspond with phase equilibrium lines for which a degree of depletion is reached of 30% and 60%. The kink at 15 GPa corresponds to the phase transition that takes place at this depth. The thick dotted line is the initial geotherm at which melting is switched on at $t = 0$ for Models A and B. For Model C, this is the thin dotted line. (b) (inset), degree of depletion (F) as function of normalized super-solidus temperature θ for the two models. The linearized curve (dashed) is a simplification of data given by Jacques and Green (1980) and corresponds with the dashed phase-lines of Fig. 2a. The bent curve (solid) is the third-order polynomial fit as determined by McKenzie and Bickle (1988) and is used in the phase-diagram given by the curved phase-lines of Fig. 2a. The dots correspond to F -values of 0, 30, 60 and 100% and for which the phase lines are given in Fig. 2a.

steady-state is used as an initial condition for a subsequent model run including partial melting and decrease of radiogenic heat production with time. We refer to previous work (De Smet et al., 1998a) for a more extensive discussion.

2.2. Parameterization of the partial melting process

Mantle differentiation through partial melting is implemented in our model based on a melting

phase-diagram for peridotite, which gives the equilibrium value of degree of depletion F for given values of p and T . In previous work (De Smet et al., 1998a) we have used a simple parameterization of the phase-diagram, using linear and parallel curves for solidus and liquidus (Takahashi and Kushiro, 1983). Here, we also apply an improved parameterization based on a higher order polynomial fit of empirical data for the solidus and liquidus of mantle peridotite. Solidus and liquidus lines for both parameterizations are shown in Fig. 2a labeled with S and L, both the linear (dashed lines) and the polynomial (solid lines) parameterizations are shown.

Up to 15 GPa the curved solidus and liquidus are third-order fits to data from Gasparik (1990) and Takahashi (1990) also used by Vlaar et al. (1994). For pressures in excess of 15 GPa, a second-order fit to the data from Ohtani et al. (1986) has been applied. The sample material used in both references are not identical and therefore a constant shift of about -70 K has been applied to the data points from Ohtani et al. (1986) such that solidus and liquidus are continuous at $p = 15$ GPa. With $\vec{p} = (1, p, p^2, p^3)^T$ the parameterization used for the solidus is:

$$T_s(p) = \vec{a}_s \vec{p}$$

$$\vec{a}_s = (1136, 134.2, -6.581, 0.1054)^T: p \leq 15 \text{ GPa}$$

$$\vec{a}_s = (1510.76, 46.27, -0.8036, 0.0)^T: p > 15 \text{ GPa}$$
(2)

where superscript T is the transposed of the vector.

For the liquidus we used:

$$T_l(p) = \vec{a}_l \vec{p}$$

$$\vec{a}_l = (1762, 57.46, -3.487, 0.0769)^T: p \leq 15 \text{ GPa}$$

$$\vec{a}_l = (1470.3025, 55.53, -0.9084, 0.0)^T:$$

$$p > 15 \text{ GPa}$$
(3)

From Fig. 2 we conclude that up to 5 GPa and near the solidus (indicated with S in Fig. 2a) both parameterizations are similar. However, for the larger part of the phase-diagram the differences are significant. Deep melting processes for pressure values exceeding 10 GPa, for example, are excluded by the

linear parameterization for realistic geotherms.

Also, the polynomial parameterization is combined with a more realistic parameterization of depletion dependency on the normalized super-solidus temperature θ given by:

$$F(p, T) = f\left(\frac{T - T_s(p)}{\Delta T_{sl}(p)}\right) = f(\theta) \quad (4)$$

where symbol definitions are given in Table 2. We adopted an empirical relation for $f(\theta)$ as given by McKenzie and Bickle (1988), which is based on a third order polynomial fit of available empirical data. In Fig. 2b, this relation is represented by the solid curve and the dash-dotted line is the linear relation used by De Smet et al. (1998a), a linear fit derived from data given by Jacques and Green (1980). The dots on the curves correspond to different degrees of depletion (30%, 60%) for which the equilibrium phase lines are drawn in Fig. 2a. The different phase diagrams result in a different distribution of partial melting. In particular, the more realistic curved solidus will result in melt production at greater depths. The differences in the phase diagrams result in different dynamics of the model. This is caused mainly by the corresponding differences in the compositional buoyancy defined in terms of F and in the differences in latent heat consumption during partial melting. The density effecting the buoyancy is given by the linearized equation of state:

$$\rho(T, F) = \rho_0 [1 - \alpha(T - T_{\text{sr}}) - F\delta\rho/\rho_0] \quad (5)$$

The EOS (Eq. (5)) includes a linear fit of empirical data specifying $\rho(F)$ from Jordan (1979), where $\delta\rho$ is given in Table 2.

In the present work, two sets of modeling results are discussed which differ in the type of parameterization of the melting phase-diagram. Model A uses the linearized parameterization and Model B and C are based on the higher order polynomial parameterization.

2.3. Thermal coupling between upper and lower mantle

For secular cooling models of the upper mantle, thermal coupling between upper and lower mantle is important. Here, we consider two limiting cases implemented in the aforementioned Models A to C.

Model A includes a simple heat reservoir representing the lower mantle which is assumed isothermal $T = T_R(t)$ as used by Kameyama et al. (1996). The reservoir does not contain any internal heating. Its volume is twice the volume of the upper mantle and other physical properties equal those of the upper mantle. The heat extracted from the reservoir is computed from the heat flux through the lower boundary of the numerical model, i.e., the upper/lower mantle interface. The reservoir temperature is used as a time-dependent essential boundary condition in Model A.

In Models B and C we consider an upper mantle thermally isolated from the lower mantle. With the heat reservoir approximation we establish a more realistic estimate of the effect of a non-zero heat flow from the lower mantle. Models with a zero heat flux condition at the bottom boundary can be considered as end-member cases, which result in a maximum estimate of the cooling rates of secular cooling of the upper mantle system (De Smet et al., 1998a).

2.4. Governing model equations and numerical methods

In the following equations, non-dimensional quantities are used unless explicitly stated otherwise. We used a non-dimensionalization scheme described by Van Den Berg et al. (1993).

For an infinite-Prandtl-number fluid, the momentum equation with the thermal and compositional Rayleigh numbers R_a and R_b respectively, is given by:

$$\nabla(\eta(\nabla\vec{u} + \nabla\vec{u}^T)) - \nabla\Delta p = (R_a T + R_b F)\hat{z} \quad (6)$$

where \hat{z} is the unit vector in the vertical direction aligned with gravity. The definitions of the symbols are listed in Table 2.

The transport equation describing partial melting of a volume of mantle material in terms of the degree of depletion F is:

$$\frac{dF(p, T)}{dt} = \frac{df(\theta)}{dt} \quad (7)$$

where the right-hand-side describes a source distribution of partial melt production following from the phase diagram discussed above. Recurrent melting is

incorporated in this formulation, meaning that a volume of recycled partially melted material experiences further melting when its super-solidus temperature θ is in excess of any previously reached value.

The energy equation used is based on the Extended Boussinesq Approximation (EBA) (Ita and King, 1994):

$$\begin{aligned} \frac{dT}{dt} - \text{Di}(T + T_0)u_z = \nabla^2 T + \mathcal{R}H(z, t) \\ + \frac{\text{Di}}{R_a}\Phi - (T + T_0)\frac{\Delta S}{c_p}\frac{dF}{dt} \end{aligned} \quad (8)$$

where the symbols are defined in Table 2. The last three terms of the right-hand-side are: the radioactive heat generation, viscous dissipation, and latent heat consumption. The second term on the left accounts for cooling and heating due to adiabatic (de-)compression. The effect of viscous heating is relatively small since the vigor of convection is low after the depleted layer has formed.

The momentum and energy equations are solved with a finite element method (Van Den Berg et al., 1993) and a time-dependent upwind scheme (SUPG) (Hughes and Brooks, 1979; Segal, 1982) is applied to the latter to improve numerical stability in advection dominated regions of the domain. The transport equation for F is solved using a Method of Characteristics (MoC) (Sotin and Parmentier, 1989; Sparks and Parmentier, 1993). A hybrid scheme using both low and high order interpolations for F in combination with a fourth order Runge–Kutta time-integration for the integration part was applied over a structured grid (De Smet et al., 1998b). In order to limit the amount of numerical diffusion over the whole domain, this unequally spaced grid used for the MoC computations of the degree of depletion field F was much denser than the finite element mesh used, and the grid densities were higher than those used by De Smet et al. (1998a). We used a resolution with grid cells ranging from 1121 to 3116 m in the horizontal direction and 921 to 1688 m in the vertical direction. A Predictor-Corrector time-stepping scheme is applied to solve the Equations in the following order: Eqs. (6)–(8).

3. Numerical modeling results

We will focus mainly on the differences in the evolution of Models A and B. Results for Model A are qualitatively similar to earlier results described by De Smet et al. (1998a). The increase of the activation volume in our present models results in a colder geotherm due to a thinner MBL. Up to approximately 200 Ma both models A and B show a similar evolution pattern. After this time deep upper mantle differentiation starts to occur in Model B.

We first discuss the early stage before the onset of deep melting in Model B. Next we describe the long term evolution of the continental model with special interest in the stability of the system. A brief description of the dynamically created initial condition has been given above.

3.1. Early evolution

From Fig. 3a and 3b a global comparison between model A and B can be made. In the left column the compositional field (degree of depletion F) is shown with upper (white) and lower (black) crustal layers on top of the partially depleted layer shown in color. The lateral variation of the temperature field with respect to the horizontally averaged background value, i.e., $T - \langle T \rangle_{\text{hor}}$, is shown in the right-hand column. All frames also contain instantaneous flow lines indicating clock- and counterclockwise flows as black and white contour lines respectively. The advection velocities in Model A are higher than those in Model B as can be seen from the number of flow lines within each convection cell. This is mainly due to the differences in the accumulated depleted layers resulting from the different melting parameterizations as will be shown below. The small down-wellings of material with low degree of depletion of < 10% (light-blue to white) in Fig. 3.b.2 are due to re-mixing as will be discussed together with the long term evolution.

The lateral temperature variations are similar for both models, with exception of the high T -anomaly above the up-welling part of the convecting cells in Fig. 3a2. This large scale two-cell convection pattern is persistent during a long period of the model

evolution. Fig. 3a and 3b illustrate the relatively short time scale of < 100 Ma in which a compositionally distinct continental root builds up in a convecting mantle after the onset of melting at $t = 0$. This shows that mantle differentiation is a powerful process in a planetary mantle which is hot enough for the mantle adiabat to intersect the solidus. The rapid build-up of a stably layered system results in a reduced heat transport efficiency and a gradual warming of the deeper half of the model.

Fig. 4 shows the depth distribution of several horizontally averaged quantities for four time values after the onset of melting for both Model A (Fig. 4a) and B (Fig. 4b). Frames numbered 1 through 4 correspond to (1) degree of depletion F , (2) temperature T , (3) viscosity $\eta(p, T)$, and (4) root-mean-squared velocity V_{rms} . The averaged profiles for F (Fig. 4a1 and 4b1) indicate that both models initially evolve in a similar way. The continental root grows due to the mechanism of intermittent small scale diapiric melting events as investigated by De Smet et al. (1998a,b) where the parameterization of Model A was used. The same mechanism is operative in Model B.

The depleted layer in model B (Fig. 3b Fig. 4b1) is thicker than in Model A where melting occurs in a greater depth interval. This is clearly shown by the difference in pressure where the initial geotherm intersects the solidus lines in Fig. 2a. This pressure difference is about 1 GPa and results after 100 Ma in a continental root extending to approximately 180 and 220 km for model A and B, respectively. Note also the finite values of F in the 350 to 500 km depth range after 200 Ma in Model B (Fig. 4b1).

Due to the different $F(\theta)$ -parameterizations, the transition from the depleted root to the deeper undepleted mantle is sharper, i.e., the slope of $\langle F \rangle_{\text{hor}}$ is steeper for Model B (Fig. 4b1) than in Model A (Fig. 4a.1). Note that the maxima of $\langle F \rangle_{\text{hor}}$ are in both cases practically identical. This is explained by the fact that for a θ of about 0.25, an F -value of about 30% is obtained in both $F(\theta)$ parameterizations. This is indicated by the proximity of θ values of the two dots for $F = 30\%$ in Fig. 2b.

Fig. 4a2, 4b2 show the horizontally averaged geotherms. Both models show an initial increase of temperature with time in the deeper half of the model. This is a result of the rapid build up of a

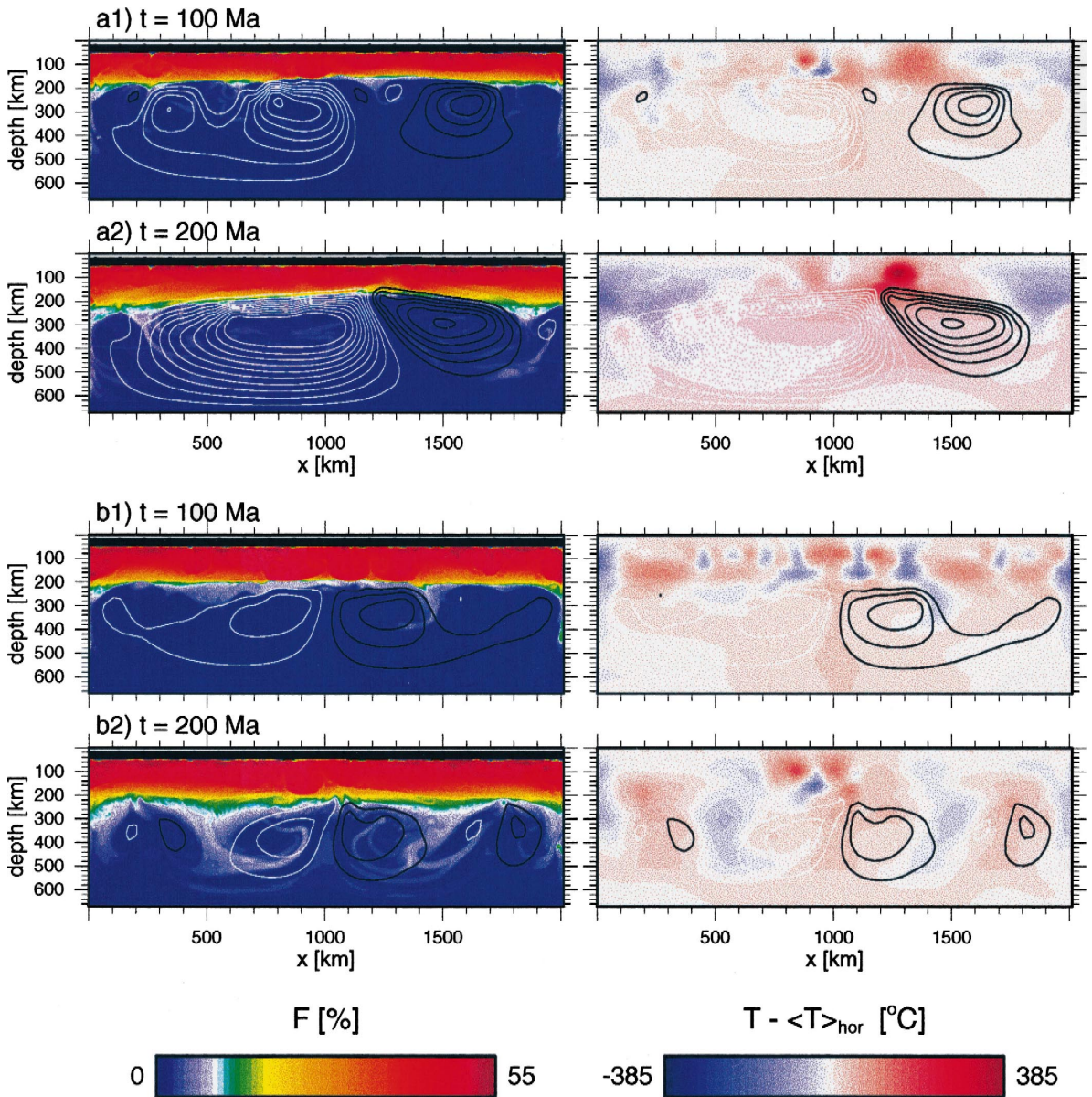


Fig. 3. The depletion field and lateral variations of the temperature field (i.e., $\delta T = T - \langle T \rangle_{\text{hor}}$) at 100 Ma and 200 Ma for both parameterizations of the phase-diagram. Figures labeled a and b correspond to Models A and B, respectively. Black and white contour lines indicate clock and counter clockwise flows, respectively. White F -field contouring corresponds to $9\% < F < 10\%$. The depletion for the polynomial case is larger than in the linear case due to the different F -dependency of θ (see the inset Fig. 2b). Also the thickness of the depleted layer is slightly thicker when the curved solidus/liquidus are used.

shallow layering inhibiting whole layer upper mantle circulation. This layering consists of cold, and therefore strong material which is part of the MBL. This cold and depleted layer is gravitationally stable with

respect to the deeper parts of the model. A super-adiabatic regime develops quickly in this stagnant top layer, indicating the predominance of conductive heat transport over advection. In Model B, the

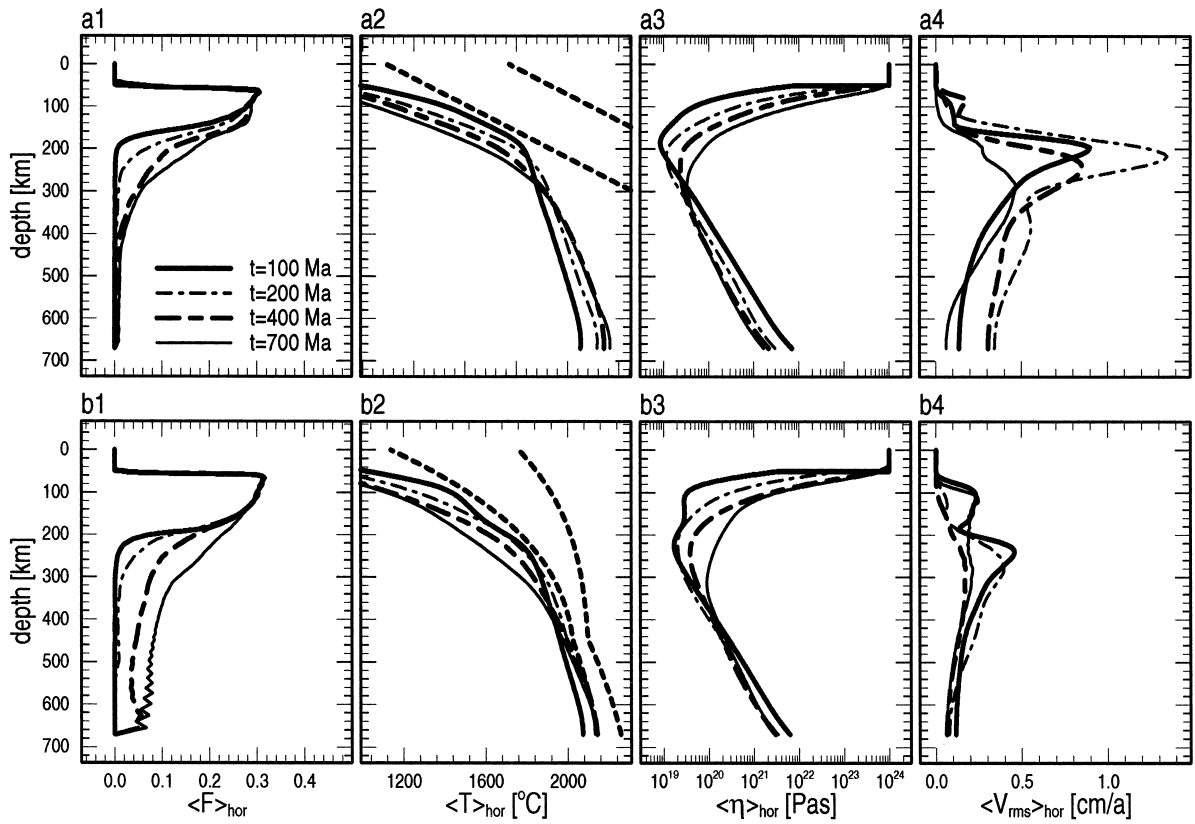


Fig. 4. For all cases shown in Figs. 3 and 5 horizontally averaged profiles are given: (1) the degree of depletion, (2) the temperature, (3) the viscosity, (4) and the velocity root mean square. The dashed curves in (a2) and (b2) are the solidus and liquidus. Note the numerical instabilities in the $\langle F \rangle$ -profile for $t = 700$ Ma in Model B (b1), which is caused by the too coarse grid over which the transport equation for F is solved. These wiggles are also expressed by the wash-board effect in Fig. 5b2.

geotherm intersects the solidus at large depths at $t \sim 200$ Ma and melting is initiated in the lower half of the domain. The latent heat effects of the endothermic phase transition from olivine to spinel at 15 GPa may prevent the geotherm from crossing the solidus above 15 GPa. However, solid-state phase transitions are not included in the present models.

After several hundred million years (~ 300 Ma) the temperature at the bottom of the upper mantle starts to decrease. These results illustrate the thermal blanketing effect of layered continental systems (Gurnis, 1988), which delay secular cooling. This decrease of the bottom temperature is stronger in Model B, because of the absence of heat influx from the lower mantle, and because latent heat consumption and surface heat flow are higher in Model B.

In Fig. 4a3,b3 viscosity profiles are shown, the crustal viscosity is set by the truncation value $\eta_{\text{max}} = 10^{24}$ Pa s applied for numerical reasons. Effects of initial warming at large depth and cooling from the top are reflected in the temperature-dependent viscosity. Model A develops a viscosity minimum which is slightly more pronounced and at shallower depth than Model B.

In Fig. 4a4,b4 we show the V_{rms} distribution based on horizontal averaging. Model B shows a strongly reduced vigor of convection in the top half of the model. This is explained by the fact that the low viscosity zone in Model A is effectively positioned below the depleted layer resulting in a relatively mobile top layer of the undepleted mantle. In Model B the low viscosity zone occupies a depth

range with finite value of the degree of depletion F , reducing the vigor of convection.

3.2. Long-term evolution

Fig. 4a1,b1 show that models A and B have a different long-term evolution. In Model A the thickness and volume of the continental root gradually increases with time due to the melting events in the upward flow of the two cell convection pattern which persists in the deep undepleted zone. At the sites of the down-wellings depleted material is slowly dragged into the lower half of the model. A low degree of depletion of about 2% volume average is found in this lower half.

In Model B much further depleted material is found in this deep region. Only a small part of it originates from re-mixed depleted material. Most of it is formed at depth since the geotherm has reached and crossed the solidus after about 200 Ma of evolution as shown in Fig. 4.b.2. This results in modest but steady partial melting during the time-span from $t = 200$ Ma to 850 Ma. The wiggles in F shown in Fig. 4b1 below 450 km depth are due to the limited grid resolution in the lower part of the model.

Fig. 4a2,b2 show the evolution of the geotherm for Models A and B, respectively. In Model B, the geotherm is stabilized close to solidus at large depths (i.e., $p > 15$ GPa) during the initial warming stage. This is the result of the occurrence of deep partial melting and the associated latent heat consumption at these depths. In Model A, the averaged temperature at 670 km is steadily increasing and is not bounded by partial melting. Due to shallower melting events the root is growing steadily and conductive heat transport slowly becomes more dominant than advection.

The geotherms in Fig. 4a2,b2 also show when the heat reservoir approach is used, i.e., Model A, the inflow of heat from the lower mantle is very small. We therefore conclude that the differences in the results of Models A and B are mainly due to the difference in the phase-diagrams and to a lesser extent to the different thermal coupling with the lower mantle. Fig. 4a3,b3 show the corresponding viscosity profiles during the evolution. In Model B the viscosity at large depths reaches an almost stationary value after 200 Ma since the geotherm be-

comes almost stationary. As secular cooling proceeds the MBL at the top grows and the minimum viscosity value increases and its position slowly shifts from 200 to 300 km depth during the 200 to 700 Ma time-span. Model A has a less thick depleted top layer and advection rates are higher than in Model B. This results in a hotter geotherm in the root and a smaller viscosity minimum.

These differences in geotherm evolution combined with a different evolution of the buoyant zone result in different convection velocity profiles shown in Fig. 4a4,b4. Fig. 4a4 shows that the vigor of convection in Model A has increased near the bottom of the depleted root. This indicates active melting and corresponding production of buoyant residual material. The thickness of the continental root grows accordingly (Fig. 4a1). After 200 Ma velocities decrease as an effect of cooling from the top and a corresponding increase of the viscosity, shown in (Fig. 4a3).

Fig. 4b4 shows a downward shift of the velocity maximum and an increase of velocity at greater depth which coincides with the onset of deep melting around 200 Ma. If we define that the transition from root to underlying mantle is situated at approximately $F = 0.1$, we see that at 700 Ma the continental root in Model B has grown to about 400 km thickness with large lateral variations (Fig. 5). Convection velocities start to increase again while the melt production in the deep layer ($p > 15$ GPa) continues. Calculations for Model B were stopped at 850 Ma because the insufficient resolution in the bottom layer and corresponding oscillations in the F -field solutions produce increasingly unreliable results beyond that time.

Fig. 5a and 5b are contour plots of the depletion and temperature fields for Models A and B, respectively. These snapshots correspond to the profiles as given in Fig. 4, i.e., 400 and 700 Ma. For Model A also the snapshot at $t = 1200$ Ma is given.

In Model A the pattern of convection changes from a relatively vigorous two-cell pattern at 400 Ma to a multi-cell convection regime at 700 Ma, in line with the observed $\langle V_{\text{rms}} \rangle_{\text{hor}}$ profiles discussed above (Fig. 4a4). Melting has stopped at ~ 650 Ma, so the depletion F is subject to advection only from that time on. Both snapshots of Model A show structures of depleted material with depletion values up to 10%

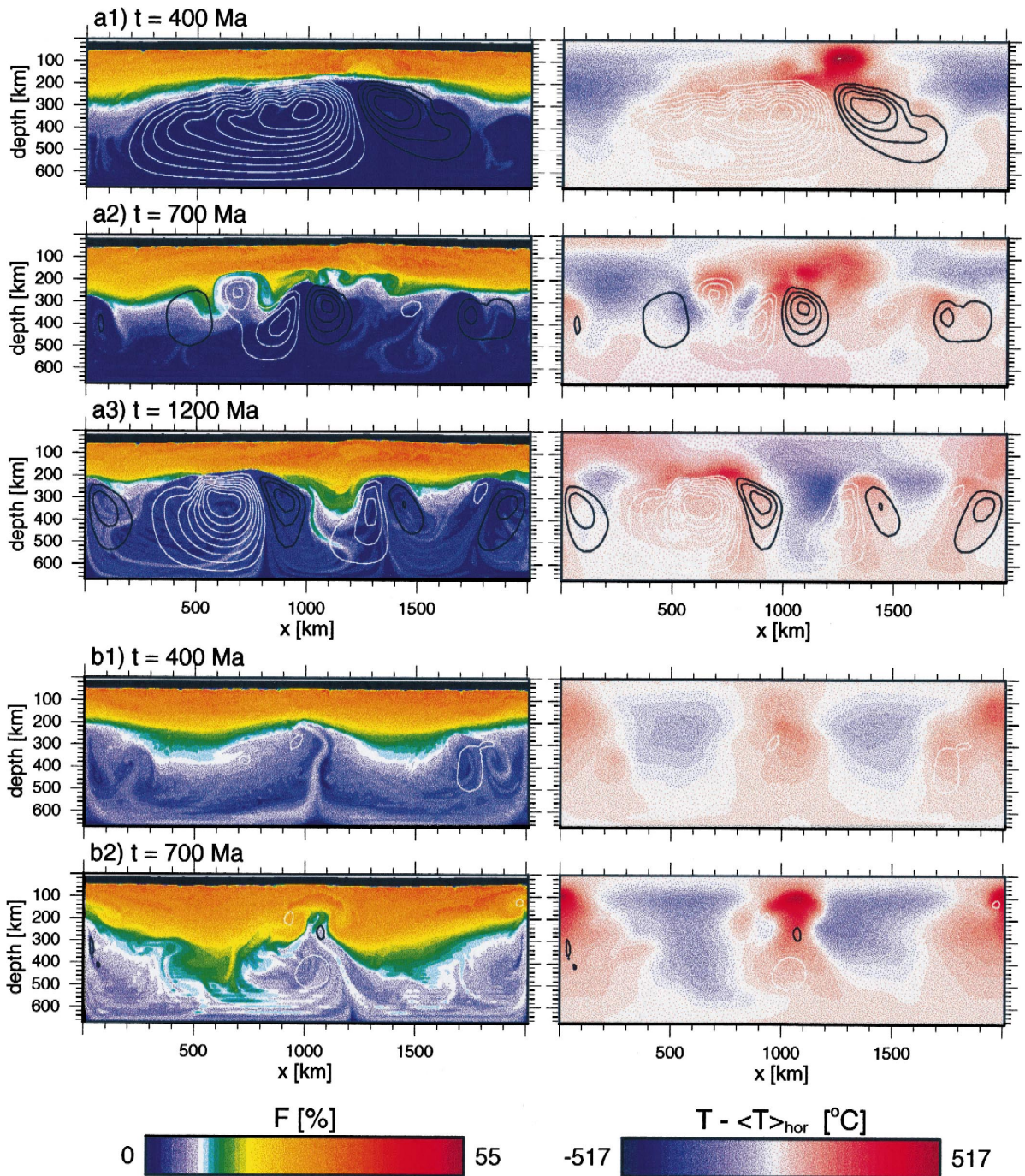


Fig. 5. As in Fig. 3 but now for $t = 400, 700$ Ma and for Model A also at 1200 Ma. Figures labeled (a) and (b) correspond to Models A and B, respectively. Due to melting at large depths in Model B the lower half of the domain is also depleted. The wash-board effects visible in the degree of depletion of Fig. 3b2 are numerical instabilities caused by the MoC-method applied over the too coarse grid in this lower part of the domain.

(white), which are dragged down into the undepleted zone. This process contaminates the deeper regions with depleted material at very slow rates. At $t = 1200$ Ma (Fig. 5a3) there is a small thread-like structure of depleted material (green, i.e., $F \sim 15\%$) delaminating at $x = 1000$ km.

Fig. 5a3 shows more stream-lines at $t = 1200$ Ma than Fig. 5a2 at $t = 700$ Ma, indicating that convection rates have increased over this time interval. This is caused by continued cooling from the top, which slowly increases the temperature difference across the deeper undepleted layer and increases convection rates. It also neutralizes the positive compositional buoyancy of the deep part of the continental root, which allows for intermittent small scale delamination (Fig. 5a3). At the same time, however, the MBL extends to larger depths due to the cooling from the top (Fig. 4a3), which prevents the gross part of the root from sinking into the slowly convecting undepleted layer.

The lateral temperature variations shown in Fig. 5a1,a2 also express the change in convection style. The high T -anomaly above the ascending flow in the two-cell convection decreases from $t = 400$ to 700 Ma.

Fig. 5b1,b2 show the same snapshots for Model B. The scarcity of the streamlines illustrates that the vigor of convection is much lower compared to Model A, which is in line with the 1-D velocity profiles shown in Fig. 4b4. The differences in the depletion fields between Models A and B are large due to the ongoing deep melt production in the latter. This is illustrated by the large amount of depleted material with $F > 10\%$ (white = 10%) advected by the convection in the deep zone. Ongoing melt production keeps adding residual material in the continental root which grows to a depth of about 400 km. The ‘wash-boarding’ effect in the low depletion zone (light blue to white) correspond to the wiggles already described in the 1-D profiles in Fig. 4b1. In Fig. 5a3, no ‘wash-boarding’ is observed since the used resolution is much higher in the lower part of the domain in Model A than in Model B.

The amplitude of the temperature anomalies in Model B increase from $t = 400$ to 700 Ma as shown in Fig. 5b1 and 5b2. This coincides with a temporal acceleration of the convective flow at about $t = 700$ Ma, related to the up-welling near $x = 1000$ km and

downward flow at $x = 500$ and 1500 km. The temperature anomalies shown in the right-hand column correlate with the distribution of composition and the structure of the convective flow. The depleted compositional root is generally cold with the exception of young newly formed residual material in up-welling flow. Both the spatial variations of depletion and of the temperature field are reflected in the geophysical observables: the seismic wave velocity structure of continental areas as revealed by surface wave tomography (Muyzert, 1996; Curtis et al., 1998), wave velocity patterns (Jordan, 1975; Anderson, 1990), and the shear wave velocity distribution on a global scale (Zhang and Tanimoto, 1993), and in the observed gravity field over continental areas (Matyska, 1994; Doin et al., 1996).

3.3. Patterns of mantle differentiation

Fig. 6a1 and 6b1 show the evolution of the melt production accumulated over columns in the models as a function of the x -location and the evolution of this melting pattern. The first 50 Ma of the evolution corresponds to the initial phase of rapid differentiation immediately following the onset of melting at $t = 0$. During this initial period most of the continental root is formed in our model. The figures show that most of the melt is formed in vertical columns with a steady position at the location of warm up-wellings in the large-scale convection pattern of the deep mantle shown in Fig. 3. Fig. 6a2,b2 show the evolution accumulated over rows of the computational domain. These frames illustrate the evolution of the melt generation at different depths. Melt production occurs in a wider range for Model B as a consequence of the different shape of the peridotite solidus (Fig. 2a).

Deep melt production for $p > 15$ GPa starts around 200 Ma in Model B (see Fig. 6b) and continues until the end of the computation at 850 Ma. The deep melting has a less pulsating character in time because this type of melting does not take place in rapid vertical ascending flows. Melt generation is concentrated at 600 km depth and near the kink of the phase equilibrium at 448 km depth, i.e., at $p = 15$ GPa. This is explained by the way in which the almost adiabatic deep geotherm intersects the curved solidus in the this part of the model. The large

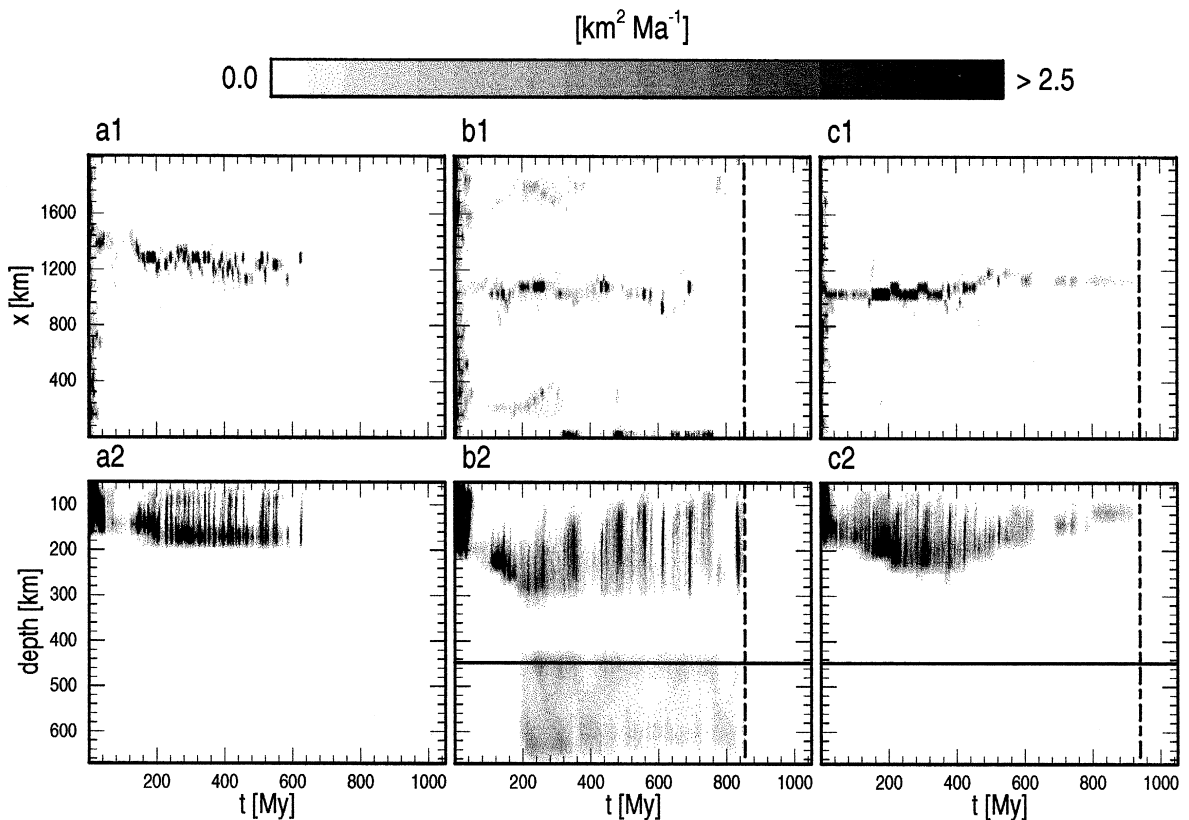


Fig. 6. The horizontal (a1–c1) and the 1-D depth (a2–c2) melt production distribution as a function of time for Model A, B and C. Figures labeled (a), (b) and (c) correspond to Models A, B and C, respectively. Note the large difference in partial melting depths for both cases. In (b2) and (c2), the solid line is the depth where the 15 GPa kink in the solidus is located. The dashed vertical lines indicate the time where computations have been stopped. Model calculations for Model A exceed the here given time-window.

melting event between 200–300 km depth at 700 Ma shown in (Fig. 6b2) is reflected in the F - and T -fields shown in (Fig. 5b2).

The same melt production plots for Model C are given in Fig. 6c1,c2. Model C has the same phase-diagram parameterization as Model B, but no deep melting occurs due to the lower potential temperature and the lower density of heat generating elements. The pattern of melting is therefore similar as in Model A and differentiation takes place at pressures lower than 10 GPa. The depth range is, however, larger than in Model A and extends to a maximum of 250 km. When cooling proceeds, melting ceases as in Model A, although in Model C melting proceeds longer than in Model A.

A 3-D extension of the 2-D model will not alter the observed processes to a great extent. On the one

hand, a cylindrical type of upwelling in a 3-D model will probably melt further since it can penetrate more easily into the existing root. On the other hand, excess heat contained in the diapir is also lost more rapid in a cylindrical configuration, which results in more modest degrees of melting.

3.4. Global evolution

Fig. 7 shows several globally averaged quantities for Models A, B and C, denoted by short dashed, solid, and long dashed lines respectively. The first –150 to 0 Ma show the statistically steady-state of the start-up scenario during which partial melting and decay of radioactive heat sources is switched off. Melting is allowed for times larger than $t = 0$ Ma, when radioactive decay starts. This results in the

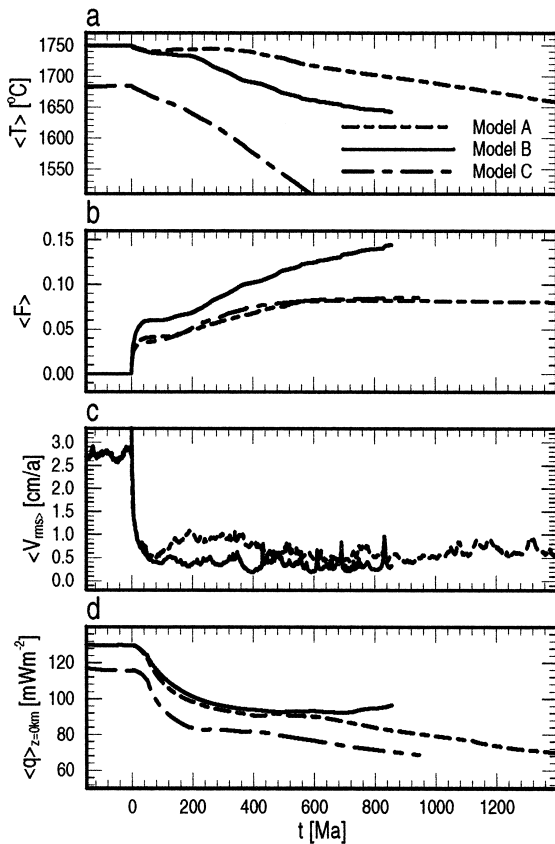


Fig. 7. For both models the evolution of some volume averaged quantities are given. The results for Model A, B and C drawn with short dashed, solid, and long dashed lines, respectively. Volume averages of the following quantities are depicted: (a) temperature, (b) degree of depletion, (c) velocity root-mean-square (Model C not shown). The averaged surface heat flow number is depicted in (d).

short period of about 50 Ma of extensive differentiation illustrated also in Fig. 6, during which a large part of the continental root is formed. The rapid initial formation is an artifact of the particular start scenario used. Subsequent evolution however shows more realistic aspects of the model.

The volume averaged temperature shown in Fig. 7a diverges between Model A and B, especially from about 200 Ma onwards. This is mainly due to the effect of latent heat consumption, which increases strongly at the onset of deep melt production in Model B. The secular cooling shown in Fig. 7a is

mainly due to conductive cooling from the top, since deeper parts of the model experience an initial warming during several hundred million years as shown in the evolution of vertical profiles in Fig. 4. Model C has an averaged initial temperature which is 70 K lower than in Models A and B. After the onset of melting, owing to the reduced heat production, the temperature in Model C drops much faster than in the two others.

Fig. 7b shows the volume average of the degree of depletion. The initial phase of rapid melting is reflected in the steep increase of $\langle F \rangle$. In Model B, more melt is produced and melting continues until the end of the computations whereas in Model A, melting ceases around $t = 650$ Ma. Model C produces approximately the same volume of continental root as Model A which is explained by the difference in phase-diagram parameterization: in spite of the colder geotherm it can still generate a large amount of depleted material.

Fig. 7c shows the root mean squared velocity V_{rms} based on the volume average. After an initial spike shortly after $t = 0$ of 5 cm a^{-1} for Models A and B, truncated in the time series plot, the $\langle V_{rms} \rangle$ drops from 2.8 cm a^{-1} during the statistically steady-state before the onset of melting to a value lower than 1 cm a^{-1} . Small local maxima correspond to pulsating diapiric events which also coincide with small shifts in the time series of $\langle F \rangle$ (i.e., increasing) and $\langle T \rangle$ (i.e., decreasing). The $\langle V_{rms} \rangle$ for Model C (not shown) depicts a similar pattern. Relative high advection rates are found before a continental root appears, although the value is lower ($\langle V_{rms} \rangle = 1.8 \text{ cm a}^{-1}$) than in Models A and B due to the thicker MBL. After the formation of the root advection rates are of the same value as in Models A and B.

The V_{rms} values are of the order of 1 cm a^{-1} . The strong decrease of the V_{rms} after the initial spin-up at $t = 0$ Ma, which corresponds to the onset of differentiation, is due to the formation of a stably stratified layering with a top layer subject to cooling from the top down. This reduces the effective depth of the convecting layer by almost a factor 2. Applying simple boundary layer theory, with $V_{rms} \sim R_a^{2/3} \sim h^2$ and h the depth of the convecting layer (Turcotte and Schubert, 1982), predicts a decrease of V_{rms} by a factor 1/4. This approximates the velocity amplitude reduction after $t = 0$ Ma as observed in Fig. 7c.

The bottom part of the model forms a relatively slowly convecting layer, and therefore has no pronounced Thermal Boundary Layer (TBL) (Fig. 4a4).

Heat flow density through the Earth's surface is shown in Fig. 7d. Values decrease considerably after the formation of a stable continental root that prevents whole layer convection. During later evolution the strong MBL grows from the top down and a more conductive regime, with reduced heat flow, develops. The increase in $\langle q \rangle$ for Model B corresponds to the acceleration in the convective heat flow at approximately $t = 700$ Ma discussed above. The heat influx from the lower mantle in Model A is less than 7.5% of the heat outflow through the surface, whereas Model B has a zero heatflow contribution from the lower mantle. Nevertheless, the surface heat flow in Model B is slightly higher than in Model A. This is due to the modestly higher advection rates in the very shallow part of the root in Model B compared to Model A (Fig. 4a4,b4), which transports heat more efficiently through this thin shallow layer. Continental heat flow values range between approximately 25 and 75 mW m⁻² at present for cratons (Pollack et al., 1993) and the here observed values should reach this range after approximately 2 to 3 Ga which is reasonable. Model C follows Model A but with an approximately constant heat flux difference of 15 to 20 mW m⁻². This is mainly due to the reduced radiogenic heat production in the crust of Model C.

4. Concluding remarks

Our numerical modeling results show that a hot convecting mantle will produce a compositional layering which is similar to the layered model of the continental tectosphere (Jordan, 1975). It is found that this layering remains stable on a time scale greater than one billion years. These results support the conclusion that present-day cratonic continental roots revealed by seismology are relicts of a hotter Archaean mantle.

We have investigated different parameterizations of the melting phase diagram of mantle peridotite. For the more realistic parameterization, we found an increase in melt production which also occurs over a larger depth range, compared to the simpler linear parameterization. This model also shows significant

partial melting in the transition zone of the upper mantle ($p > 15$ Gpa), for a sufficiently high initial potential temperature (Model B). This model needs to be explored further in the future. In particular the solid state exothermic phase transition near 400 km depth and the associated latent heat effects on warm diapiric up-wellings and the occurrence of deep melting requires further investigation.

Simulations with a simple melting phase diagram show a compositional layering that becomes more pronounced until partial melting stops at about 650 Ma, which result from a progressive secular cooling that eventually brings the average geotherm below the solidus. This resulting layering remains stable for the duration of the computations (1400 Ma), but some small-scale delamination of the continental root and re-mixing of depleted material is observed. In the interpretation of the observed long-term stability of the continental layering, we should keep in mind some limitations of the model. In the real Earth, continents break up. This may be related to the interaction of large scale mantle plumes with continental roots and a certain degree of freedom for continental blocks to migrate laterally (Ebinger and Sleep, 1998). In our model, lateral migration is limited by the symmetry condition applied on the vertical boundaries of the computational domain. At the same time, only relatively small mantle diapirs interact with the continental root and they cannot sufficiently affect the root to result in continental break up.

The continental root grows by means of relatively small scale diapiric up-wellings which cross the solidus near the lower boundary of the root. These diapiric flows are then accelerated by the density reduction effect of the partial melting process on the residual matrix, resulting in a positive buoyancy which dominates the effects of latent heat consumption and adiabatic decompression, both included in our models. The amount of melt produced in a single diapiric event is significantly smaller than the estimated amounts produced during events that are related to continental flood basalts.

A clear correlation was found between lateral variations of the temperature and of the thickness of the continental root. Cold areas coincide with an increased thickness of the root and warm areas show a thinned root.

Acknowledgements

We thank Shijie Zhong and Rob van der Hilst for critical reviews which helped to improve the manuscript. We acknowledge stimulating discussions with David Yuen. This work was partly supported by the Netherlands Organization for Scientific Research (NWO) and the Dr. Schürmann foundation through travel grants and was partly carried out during a visit of Jeroen de Smet and Arie van den Berg at the Minnesota Supercomputer Institute. Support was also received from the Netherlands Science Foundation (NWO) and NATO.

References

- Anderson, D.L., 1990. Geophysics of the continental mantle: a historical perspective. In: Menzies, M. (Ed.), *Continental Mantle*. Oxford, United Kingdom, Clarendon Press, pp. 1–30.
- Chapman, D.S., 1986. Thermal gradients in the continental crust. In: Dawson, J.B., Carswell, D.A., Hall, J., Wedepohl, K.H. (Eds.), *The Nature of the Lower Continental Crust*. Vol. 24, Spec. Publ. Geol. Soc. London, pp. 63–70.
- Condie, K.C., 1984. Archaean geotherms and supra crustal assemblages. *Tectonophysics* 105, 29–41.
- Curtis, A., Dost, B., Trampert, J., Snieder, R., 1998. Eurasian fundamental mode surface wave phase velocities and their relationship with tectonic features. *J. Geophys. Res.* 103, 26919–26947.
- De Smet, J.H., Van Den Berg, A.P., Vlaar, N.J., 1998a. Stability and growth of continental shields in mantle convection models including recurrent melt production. *Tectonophysics* 296, 15–29.
- De Smet, J.H., Van Den Berg, A.P., Vlaar, N.J., 1998b. A characteristic based method for solving the transport equation and its application to the process of mantle differentiation and continental root growth (submitted to *Geoph. J. Int.*).
- Doin, M.-P., Fleitout, L., Christensen, U., 1997. Mantle convection and stability of depleted and undepleted continental lithosphere. *J. Geophys. Res.* 102, 2771–2787.
- Doin, M.-P., Fleitout, L., McKenzie, D., 1996. Geoid anomalies and structure of continental and oceanic lithospheres. *J. Geophys. Res.* 101, 16119–16135.
- Dupeyrat, L., Sotin, C., Parmentier, E.M., 1995. Thermal and chemical convection in planetary mantles. *J. Geophys. Res.* 100, 497–520.
- Ebinger, C.J., Sleep, N.H., 1998. Cenozoic magmatism throughout East Africa resulting from impact of a single plume. *Nature* 395, 788–791.
- Gasparik, T., 1990. Phase relations in the transition zone. *J. Geophys. Res.* 95 (B10), 15751–15769.
- Gurnis, M., 1988. Large-scale mantle convection and the aggregation and dispersal of supercontinents. *Nature* 332, 695–699.
- Hirth, G., Kohlstedt, D.L., 1996. Water in the oceanic upper mantle: implications for rheology, melt extraction and the evolution of the lithosphere. *Earth Planet. Sci. Lett.* 144, 93–108.
- Hughes, T.J.R., Brooks, A., 1979. A multidimensional upwind scheme with no crosswind diffusion. In: Hughes, T.J.R. (Ed.), *Finite Element Methods for Convection Dominated Flows*, Vol. 34 of Applied Mechanics Division, American Society of Mechanical Engineers, New York.
- Ita, J., King, S.D., 1994. Sensitivity of convection with endothermic phase change to the form of governing equations, boundary conditions and equation of state. *J. Geophys. Res.* 99, 15919–15938.
- Jacques, A.L., Green, D.H., 1980. Anhydrous melting of peridotite at 0–15 kb pressure and genesis of tholeiitic basalts. *Contrib. Mineral. Petrol.* 73, 287–310.
- Jordan, T.H., 1975. The continental tectosphere. *Geophys. Space Phys.* 133, 1–12.
- Jordan, T.H., 1979. Mineralogies, densities, and seismic velocities of garnet lherzolites and their geophysical implications. In: Boyd, F.R., H.O.A., Meyer (Eds.), *The Mantle Sample: Inclusions in Kimberlites and Other Volcanics*, American Geophysical Union, Washington DC, pp. 1–14.
- Jordan, T.H., 1988. Structure and formation of the continental tectosphere. *J. Petrol.*, Special Lithosphere Issue, 11–37.
- Kameyama, M., Fujimoto, H., Ogawa, M., 1996. A thermo-chemical regime in the upper mantle in the early Earth inferred from a numerical model of magam-migration in a convecting upper mantle. *Phys. Earth Planet. Inter.* 94, 187–215.
- Karato, S., 1990. The role of hydrogen in the electrical conductivity of the upper mantle. *Nature* 347, 272–273.
- Karato, S., Jung, H., 1998. Water, partial melting and the origin of the seismic low velocity and high attenuation zone in the upper mantle. *Earth Planet. Sci. Lett.* 157, 193–207.
- Karato, S., Wu, P., 1993. Rheology of the upper mantle: a synthesis. *Science* 260, 771–778.
- Leitch, A.M., Davies, G.T., Wells, M., 1998. A plume head melting under a rifting margin. *Earth and Planetary Science Lett.* 161, 161–177.
- Lenardic, A., 1997. On the heat flow variation from archaic cratons to Proterozoic mobile belts. *J. Geophys. Res.* 102, 709–721.
- Matyska, C., 1994. Topographic masses and mass heterogeneities in the upper mantle. *Gravimetry and Space Techniques Applied to Geodynamics and Ocean Dynamics*, Vol. 17 of Geophysical Monograph Series, American Geophysical Union, Washington, DC, pp. 125–132.
- McKenzie, D., 1984. The generation and compaction of partially molten rock. *J. Geophys. Res.* 89, 713–765.
- McKenzie, D., Bickle, M., 1988. The volume and composition of melt generated by extension of the lithosphere. *J. Geophys. Res.* 93, 625–679.
- Moresi, L., Solomatov, V., 1997. Mantle convection with a brittle lithosphere: thoughts on the global tectonic styles of the Earth and Venus. *Geophys. J. Int.*, (submitted).
- Müller, R.D., Roest, W.R., Royer, J.Y., Gahagan, L.M., Sclater, J.G., 1996. Age of the ocean floor. Technical Report MGG-12,

- World Data Center A for Marine Geology and Geophysics, 325 Broadway, Boulder, CO 80303-3328, USA.
- Muyzert, E., 1996. A seismic cross section through the east European continent. *Geophys. J. Int.* (submitted).
- O'Connell, R.J., Hager, B.H., 1980. On the thermal state of the Earth. In: Dziewonski, A.M., Boschi, E. (Eds.), *Phys. Earth's Int.* Elsevier, New York, pp. 270–317.
- Ogawa, M., 1994. Effects of chemical fractionation of heat-producing elements on mantle evolution inferred from a numerical model of coupled magmatism-mantle convection system. *Phys. Earth Planet. Int.* 83, 101–127.
- Ohtani, E., Kato, T., Sawamoto, H., 1986. Melting of a model chondritic mantle to 20 GPa. *Nature* 322, 352–353.
- Polet, J., Anderson, D.L., 1995. Depth extent of cratons as inferred from tomographic studies. *Geology* 23 (3), 205–208.
- Pollack, H.N., Hurter, S.J., Johnson, J.R., 1993. Heat flow from the Earth's interior: analysis of the global data set. *Rev. Geophys.* 31, 267–280.
- Ranalli, G., 1991. The microphysical approach to mantle rheology. In: Sabadini, R. et al. (Eds.), *Glacial Isostasy, Sea-Level and Mantle Rheology*, Kluwer, The Netherlands, pp. 343–378.
- Ribe, N.M., Christensen, U.R., 1994. Melt generation by plumes; a study of Hawaii volcanism. *J. Geophys. Res.* 99, 669–682.
- Schmeling, H., Bussod, G.Y., 1996. Variable viscosity convection and partial melting in the continental asthenosphere. *J. Geophys. Res.* 101, 5411–5423.
- Schott, B., Schmeling, H., 1998. Delamination and detachment of a lithospheric root. *Tectonophysics* (submitted).
- Segal, A., 1982. Aspects of numerical methods for elliptic singular perturbation problems. *SIAM J. Sci. Stat. Comput.* 3 (3), 327–349.
- Sotin, C., Parmentier, E.M., 1989. Dynamical consequences of compositional and thermal density stratification beneath spreading centers. *Geophys. Res. Lett.* 16, 835–838.
- Sparks, D.W., Parmentier, E.M., 1993. The structure of three-dimensional convection beneath oceanic spreading centers. *Geophys. J. Int.* 112, 81–91.
- Takahashi, E., 1990. Speculations on the Archean mantle: missing link between komatiite and depleted garnet peridotite. *J. Geophys. Res.* 95, 15941–15954.
- Takahashi, E., Kushiro, I., 1983. Melting of a dry peridotite at high pressure and basalt magma genesis. *Am. Miner.* 68, 859–879.
- Turcotte, D.L., Schubert, G., 1982. *Geodynamics; Applications of continuum physics to geological problems*. Wiley.
- Van Den Berg, A.P., Van Keken, P.E., Yuen, D.A., 1993. The effects of a composite non-Newtonian and Newtonian rheology on mantle convection. *Geophys. J. Int.* 115, 62–78.
- Vlaar, N.J., Van Den Berg, A.P., 1991. Continental evolution and Archean sea-level. Sabadini, R. et al. (Eds.), *Glacial Isostasy, Sea-Level and Mantle Rheology*, Elsevier, The Netherlands, pp. 637–662.
- Vlaar, N.J., Van Keken, P.E., Van Den Berg, A.P., 1994. Cooling of the Earth in the Archaean; consequences of pressure-release melting in a hotter mantle. *Earth Planet. Sci. Lett.* 121, 1–18.
- Walzer, U., Hendel, R., 1997. Time-dependent thermal convection, mantle differentiation and continental-crust growth. *Geophys. J. Int.* 130, 303–325.
- Zhang, Y.-S., Tanimoto, T., 1993. High-resolution global upper mantle structure and plate tectonics. *J. Geophys. Res.* 98, 9793–9823.